

# Spin-orbit coupling and crystal-field splitting in Ti-doped $\text{Ca}_2\text{RuO}_4$ studied by ellipsometry

I. Vergara,<sup>1</sup> M. Magnaterra,<sup>1</sup> J. Attig,<sup>2</sup> S. Kunkemöller,<sup>1</sup> D.I. Khomskii,<sup>1</sup> M. Braden,<sup>1</sup> M. Hermanns,<sup>3,4</sup> and M. Grüninger<sup>1</sup>

<sup>1</sup>*Institute of Physics II, University of Cologne, 50937 Cologne, Germany*

<sup>2</sup>*Institute for Theoretical Physics, University of Cologne, 50937 Cologne, Germany*

<sup>3</sup>*Department of Physics, Stockholm University, AlbaNova University Center, SE-106 91 Stockholm, Sweden*

<sup>4</sup>*Nordita, KTH Royal Institute of Technology and Stockholm University, SE-106 91 Stockholm, Sweden*

(Dated: March 24, 2022)

In  $\text{Ca}_2\text{RuO}_4$ , the competition of spin-orbit coupling  $\zeta$  and tetragonal crystal field splitting  $\Delta_{\text{CF}}$  has been discussed controversially for many years. The orbital occupation depends on  $\Delta_{\text{CF}}/\zeta$ , which allows us to address this ratio via the optical spectral weights of the lowest intersite Mott-Hubbard excitations. We study the optical conductivity of  $\text{Ca}_2\text{Ru}_{0.99}\text{Ti}_{0.01}\text{O}_4$  in the range of 0.75 – 5 eV by ellipsometry, using the large single crystals that can be grown for small Ti concentrations. Based on a local multiplet calculation, our analysis results in  $2.4 \leq \Delta_{\text{CF}}/\zeta \lesssim 4$  at 15 K. The dominant crystal field yields a ground state close to  $xy$  orbital order but spin-orbit coupling is essential for a quantitative description of the properties. Furthermore, we observe a pronounced decrease of  $\Delta_{\text{CF}}$  with increasing temperature, as expected based on the reduction of octahedral distortions.

## I. INTRODUCTION

In 5d transition-metal compounds, the interplay of strong spin-orbit coupling and electronic correlations gives rise to novel electronic phases [1–5]. In materials with a partially filled 4d shell, spin-orbit coupling is much smaller, which may shift the balance in the competition between spin-orbit coupling, crystal field, electronic correlations, and exchange interactions [6]. We focus on the layered 4d<sup>4</sup> compound  $\text{Ca}_2\text{RuO}_4$  which features a temperature-driven metal-insulator transition at  $T_{\text{MI}} = 357$  K [7, 8] and antiferromagnetic (AF) order below the Néel temperature  $T_N = 110$  K [9]. Remarkably, it can be driven into a conducting non-equilibrium phase by small electric fields or currents [10–14]. The phase diagram of  $\text{Ca}_{2-x}\text{Sr}_x\text{RuO}_4$  is rich [15–20] even though the formal valence of  $\text{Ru}^{4+}$  is independent of  $x$ , pointing towards a prominent role of the  $x$ -dependent tilt and rotation angles of the  $\text{RuO}_6$  octahedra [21]. The most controversially discussed issue in  $\text{Ca}_2\text{RuO}_4$  is the relative size of spin-orbit coupling  $\zeta = 2\lambda$  and tetragonal crystal field splitting  $\Delta_{\text{CF}}$ , which affects for instance the characters of the magnetic moments and of the magnetic excitations [22–33].

In the limit  $\zeta = 0$  with  $\Delta_{\text{CF}} > 0$ , the tetragonal crystal field favors a spin  $S = 1$  state with double occupancy of the  $xy$  orbital, so-called  $xy$  orbital order, which has been found in several first-principles studies [34–36]. In the  $S = 1$  picture, spin-orbit coupling is treated as a perturbation. Early evidence for its relevance was provided by an x-ray absorption study [37] of the orbital occupation. In this picture, the highly anomalous spin-wave dispersion can be well described by large single-ion anisotropy terms [24, 28, 29]. In the opposite limit  $\Delta_{\text{CF}} = 0$  and finite  $\zeta$ , the local  $t_{2g}^4$  configuration adopts a  $J = 0$  ground state with equal population of the three  $t_{2g}$  orbitals. In fact, the ground state of a single-site model is a singlet for *any* value of  $\Delta_{\text{CF}}/\zeta$ , see Fig. 1. Such a non-magnetic ground state is realized in 5d<sup>4</sup> iridates with dominant spin-orbit coupling [38, 39]. In this case, van-Vleck-type excitonic magnetism, or singlet magnetism [40], may arise if exchange interactions are strong enough to allow for condensation of the dispersive lowest excited state [22, 23, 41]. In this picture, spin-orbit

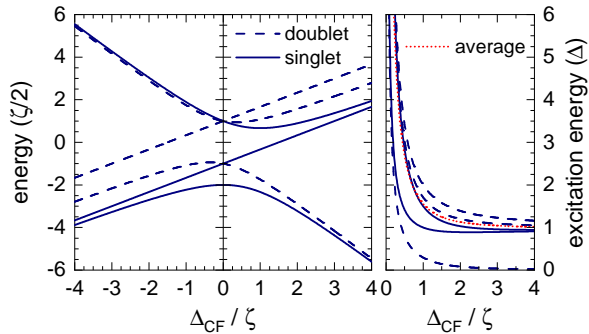


FIG. 1. Left: Energies of the nine low-energy states for a single  $t_{2g}^4$  site with Coulomb interactions, spin-orbit coupling  $\zeta$ , and tetragonal crystal-field splitting  $\Delta_{\text{CF}}$ . For  $\Delta_{\text{CF}} = 0$ , the states group into  $J = 0, 1$ , and 2. For  $\Delta_{\text{CF}} \gg \zeta$ , the three lowest states extrapolate to the  $S = 1$  triplet with double occupancy of the  $xy$  orbital. Right: Excitation energies. Red dotted line shows the average of the upper four energies.

coupling allows for a longitudinal magnetic mode that corresponds to amplitude fluctuations equivalent to a Higgs mode [22, 26, 27, 30].

Excitonic magnetism initially was proposed for the cubic case with  $\Delta_{\text{CF}} = 0$  [22] but its realization is facilitated by reducing the energy of the lowest excited state with increasing  $\Delta_{\text{CF}}/\zeta$  [23, 32], see Fig. 1. For  $\text{Ca}_2\text{RuO}_4$ , the two controversially discussed scenarios hence are aiming to describe two sides of the same coin. On the one hand, LDA+DMFT finds that dominant  $xy$  orbital order prevails in the presence of spin-orbit coupling and the spin-wave dispersion can be described by interacting local moments in an  $S = 1$  low-energy model with pronounced single-ion anisotropy [24, 28, 29]. Concerning the electronic structure as observed in ARPES, an extension of the anisotropic  $S = 1$  picture to a  $t$ - $J$ -like model describes the less dispersive bands with  $xz/yz$  character [42, 43]. On the other hand, any calculation starting from a single site and local multiplets with Coulomb interactions has to deal with the  $J = 0$  character of the lowest local state. The central quantity of the single-site model is the ra-

tio  $\Delta_{\text{CF}}/\zeta$  which determines the wavefunctions of the local low-energy states. From theory,  $\Delta_{\text{CF}}/\zeta \approx 3$  was obtained in LDA+DMFT [29]. The analysis of on-site  $dd$  excitations observed at 12 K by resonant inelastic x-ray scattering (RIXS) at the Ru  $L$  edge [44] yields  $\zeta = 0.13$  eV and  $\Delta_{\text{CF}}/\zeta = 2$ . In this parameter range, the local  $J=0$  ground state shows dominant occupation of the  $xy$  orbital and the energy scale of the lowest excitations is small,  $(\zeta/2)^2/\Delta_{\text{CF}}$ .

We demonstrate that optical measurements provide a sensitive tool to determine  $\Delta_{\text{CF}}/\zeta$  in  $4d$  compounds. We employ ellipsometry which profits from the availability of large crystals since the oblique angle of incidence reduces the effective sample size. In-depth studies of  $\text{Ca}_2\text{RuO}_4$  were hampered for a long time by the small size of the available single crystals. Upon cooling down after crystal growth, the samples typically pulverize at the metal-insulator transition at  $T_{\text{MI}} = 357$  K due to large accompanying jumps of the lattice parameters [21]. Substituting 1 % of the Ru ions by Ti ions broadens the phase transition, keeping the crystals intact, while  $T_{\text{MI}}$  and structural and magnetic properties such as the Néel temperature  $T_N$  are hardly affected [25].

In  $\text{Ca}_2\text{Ru}_{0.99}\text{Ti}_{0.01}\text{O}_4$ , we address  $\Delta_{\text{CF}}/\zeta$  via the spectral weight of Mott-Hubbard excitations  $|4d_i^4, 4d_j^4\rangle \rightarrow |4d_i^3, 4d_j^5\rangle$  between Ru sites  $i$  and  $j$ . In the strong-coupling limit  $t \ll U$  with hopping  $t$  and intra-orbital Coulomb repulsion  $U$ , the dipole matrix element is proportional to  $t$  and probes the same microscopic hopping processes that are relevant for magnetic exchange interactions. Based on selection rules, the optical spectral weight is sensitive to spin and orbital correlations between nearest neighbors [45–48], as observed in many  $3d$  transition-metal compounds [49–58]. In a similar way, spin and orbital correlations determine the RIXS intensity of inter-site excitations studied at the O  $K$  edge in  $3d$  transition-metal oxides [59, 60]. *A priori*, it is not clear in how far this strong-coupling approach based on local atomic multiplets works in  $4d$  systems with larger bandwidth. However, optical data as well as electron energy loss spectroscopy (EELS) demonstrate the sensitivity to nearest-neighbor spin correlations in the  $4d^5$  Kitaev material  $\alpha\text{-RuCl}_3$  [61, 62]. In  $\text{Ca}_2\text{RuO}_4$  with  $t_{2g}^4$  configuration, the optical conductivity  $\sigma_1(\omega)$  shows a pronounced temperature dependence but due to different assignments of the observed features different conclusions were drawn for the orbital occupation [34, 63]. However, spin-orbit coupling has been neglected in the analysis thus far. We analyze the lowest Mott-Hubbard excitations using a local multiplet picture and show that the optical spectral weight can be used to estimate  $\Delta_{\text{CF}}/\zeta$ . Furthermore, the optical excitation energies indicate a substantial temperature dependence of  $\Delta_{\text{CF}}$ , in agreement with the temperature dependence of the tetragonal distortion of the  $\text{RuO}_6$  octahedra [21, 25], suggesting that  $\Delta_{\text{CF}}/\zeta$  is reduced at elevated temperature.

## II. EXPERIMENTAL METHODS

Single crystals of  $\text{Ca}_2\text{Ru}_{0.99}\text{Ti}_{0.01}\text{O}_4$  (space group  $Pbca$ ) have been grown using the floating-zone method and were characterized by powder and single-crystal x-ray diffrac-

tion and measurements of the magnetization and the resistivity [25]. At room temperature, the lattice constants are  $a = 5.4098(3)$  Å,  $b = 5.4683(4)$  Å, and  $c = 11.9781(9)$  Å [25], very similar to the values found in pristine  $\text{Ca}_2\text{RuO}_4$  [9, 21]. Ellipsometric data were measured on a polished  $ab$  surface of a sample with  $4 \times 4 \times 1$  mm<sup>3</sup> in the energy range 0.75–5 eV. We use a rotating-analyzer ellipsometer (Woollam VASE) equipped with a retarder between polarizer and sample. Data were collected from 15 K to 300 K using a UHV cryostat with  $p < 10^{-9}$  mbar. The angle of incidence equals 70°. We corrected window effects by measuring a standard Si wafer for calibration. We studied an untrinned single crystal but could not resolve any anisotropy within the  $ab$  plane. The  $c$  axis is normal to the sample surface and contributes little to the data, the pseudo-dielectric function hence provides a reasonable estimate of the response within the  $ab$  plane [64]. We demonstrate in Appendix A that considering the anisotropy explicitly yields a very similar result, in particular for the properties that we address in our theoretical calculations. In the analysis, a thin surface layer with a thickness of 4 nm was included in order to account for the surface roughness.

## III. OPTICAL CONDUCTIVITY

The optical conductivity  $\sigma_1(\omega)$  of  $\text{Ca}_2\text{Ru}_{0.99}\text{Ti}_{0.01}\text{O}_4$  shows four peaks at about 1 eV, 2 eV, 3 eV, and 5 eV, see Fig. 2a. Overall, our data agree very well with previous results for  $\text{Ca}_2\text{RuO}_4$  based on a Kramers-Kronig analysis of reflectivity data [34, 63]. The substitution of 1 % of  $\text{Ru}^{4+}$  ions by  $\text{Ti}^{4+}$  ions has negligible effect on the optical properties, in agreement with the results obtained for other properties [25]. Optical data of  $\text{Ca}_2\text{RuO}_4$  were reported for 300 K by Lee *et al.* [63] and for 10 K, 250 K, 293 K, 350 K, and 370 K by Jung *et al.* [34]. The detailed temperature dependence, in particular in the vicinity of the Néel temperature  $T_N = 110$  K [9], has not been addressed thus far.

The analysis of the spectral weight is hampered if different excitations overlap. Therefore we focus on the two features with the lowest excitation energy, peaks A and B. These are identified as Mott-Hubbard excitations, while charge-transfer excitations set in at about 3 eV [34, 63], see Sect. IV. To analyze the temperature dependence, we show  $\sigma_1$  at 1.0 eV and 2.4 eV in the insets of Fig. 2a and the difference spectra  $\Delta\sigma_1 = \sigma_1(T) - \sigma_1(15\text{ K})$  in Fig. 2b. Peak A shows a remarkable increase of spectral weight with increasing temperature. Between 15 K and 300 K, its peak value increases by about a factor 2 while  $\sigma_1(1\text{ eV})$  rises by almost a factor 3. In contrast,  $\sigma_1(2.4\text{ eV})$  shows a small step like decrease upon crossing  $T_N$ , characterizing the behavior in the range 2.0–2.5 eV. Furthermore, the data show a temperature-driven broadening of the charge-transfer gap around 3 eV.

For a quantitative analysis, the complex ellipsometry data were fitted using an oscillator model. For peaks A and B, we employ two Gaussian oscillators. The asymmetric line shape of the charge-transfer gap around 3 eV is well described by two Tauc-Lorentz oscillators, and two further Gaussians are used at higher energy. According to the fit, the spectral weight

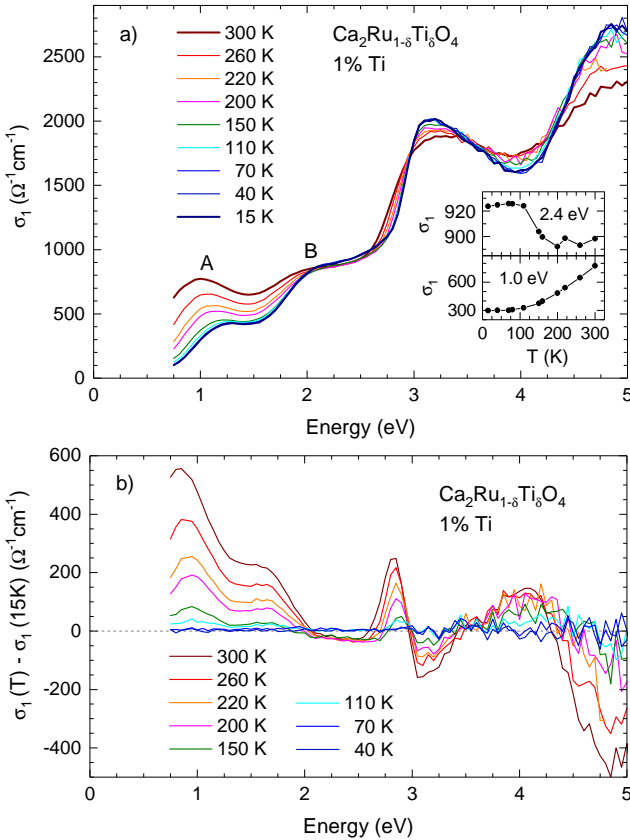


FIG. 2. a) Optical conductivity of  $\text{Ca}_2\text{Ru}_{0.99}\text{Ti}_{0.01}\text{O}_4$ . Insets:  $\sigma_1$  at 1 eV and 2.4 eV. b) Difference spectra obtained by subtracting the 15 K data. The spectral weight of peak A strongly increases with increasing temperature. Note that the shoulder at 1.2 eV at high temperature coincides with the peak energy at low temperature, i.e., it reflects the energy shift of peak A rather than two separate features.

$\text{SW}_A$  of peak A increases by a factor of about 2.2 between 15 K and 300 K, see right panel of Fig. 3, in agreement with previous results [34]. Moreover, the fit result is corroborated by direct integration of  $\sigma_1(\omega)$  between 0.75 eV and 1.5 eV. For peak B, the fit yields an increase of spectral weight  $\text{SW}_B$  by a factor 1.5, even though the peak value does not vary strongly with temperature. Also direct integration from 1.5 eV to 2.25 eV yields a weaker temperature dependence. The increase of the fit result for  $\text{SW}_B$  is mainly due to the enhanced width, making it more difficult to distinguish different features at high temperature.

For a comparison with theory (see below), the ratio  $\text{SW}_A/\text{SW}_B$  is most interesting. We focus on the value at 15 K, where the fit yields  $\text{SW}_A/\text{SW}_B \approx 0.30$ . In detail, this result depends on the assumptions for the line shape of the strong feature at 3 eV, see Fig. 4. Therefore, we performed a further fit in which the two Tauc-Lorentz oscillators were replaced by Gaussian oscillators. In this case, we find  $\text{SW}_A/\text{SW}_B \approx 0.27$ . We hence consider  $\text{SW}_A/\text{SW}_B \approx 1/3$  to  $1/4$  at 15 K.

The peak energies  $\hbar\omega_i$  for  $i = A, B$  are depicted in the left panel of Fig. 3. From 15 K to 300 K,  $\omega_B$  changes by 7 % while peak A softens by about 0.3 eV or 30 %. A similar change

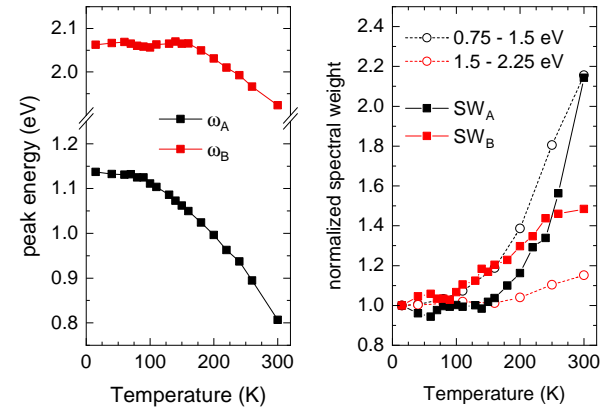


FIG. 3. Left: Energies  $\hbar\omega_i$  of peaks A and B as determined by an oscillator fit. Right: Spectral weight of peaks A and B, normalized to the 15 K value. Full symbols show the fit result, open symbols correspond to the integral of  $\sigma_1(\omega)$  over the indicated ranges.

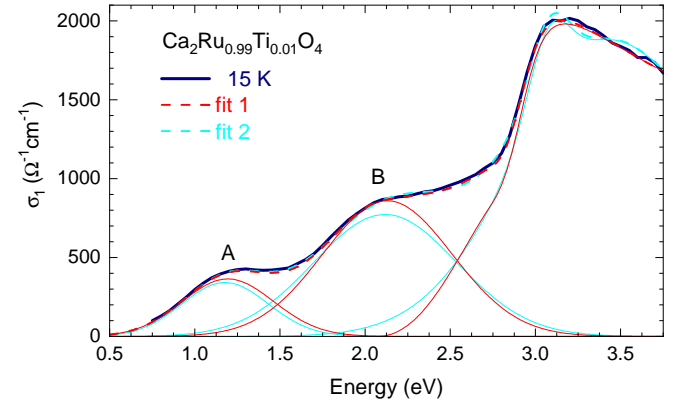


FIG. 4. Two different oscillator fits of the 15 K data. Fit 1 (red) uses two Tauc-Lorentz oscillators for the 3 eV feature, fit 2 (cyan) two Gaussian oscillators in the same range. Dashed lines show the total fit, thin lines depict the contributions of the Gaussian oscillators for peaks A and B as well as the sum of the other terms. For the spectral weight ratio  $\text{SW}_A/\text{SW}_B$  we find 0.30 in fit 1 and 0.27 in fit 2.

of 0.24 eV was reported for peak A in  $\text{Ca}_{2-\delta}\text{Sr}_\delta\text{RuO}_4$  for  $\delta = 0.06$  [63]. We will argue below that the strong temperature dependence of  $\omega_A$  and  $\Delta\omega = \omega_B - \omega_A$  reflect the pronounced reduction of the tetragonal crystal-field splitting  $\Delta_{\text{CF}}$ .

## IV. PEAK ASSIGNMENT

### A. Charge-transfer excitations

We distinguish Mott-Hubbard excitations between Ru sites and charge-transfer excitations between Ru and O sites. The latter show larger spectral weight and, in  $\text{Ca}_2\text{RuO}_4$ , contribute above about 3 eV [34, 63], in agreement with angle-resolved photoelectron spectroscopy (ARPES) showing the onset of O bands about 2.5 eV below the Fermi level [42]. The charge-transfer peak at 3 eV [34, 63] can be attributed to an elec-

tron transfer to the Ru  $t_{2g}$  shell,  $|\text{Ru } t_{2g}^4, \text{O } 2p^6\rangle \rightarrow |\text{Ru } t_{2g}^5, \text{O } 2p^5\rangle$ . The peak at 5 eV predominantly corresponds to excitations into the Ru  $e_g$  shell to a  $|\text{Ru } t_{2g}^4 e_g^1, \text{O } 2p^5\rangle$  final state. Compared to the  $t_{2g}^5$  peak at 3 eV, the larger spectral weight agrees with the enhanced hopping matrix elements between O  $2p$  and Ru  $e_g$  states. The energy difference of about 2 eV between the peaks in  $\sigma_1(\omega)$  is similar to the  $t_{2g} - e_g$  splitting observed in x-ray absorption or resonant inelastic x-ray scattering [44, 65, 66].

## B. Mott-Hubbard excitations

For the assignment of the Mott-Hubbard excitations  $|d_i^4, d_j^4\rangle \rightarrow |d_i^3, d_j^5\rangle$  between Ru sites  $i$  and  $j$ , we address the  $d^3$ ,  $d^4$ , and  $d^5$  states in a local multiplet scenario [28, 46]. The cubic crystal-field splitting 10 Dq is large enough to break Hund's rule. We thus may neglect the  $e_g$  orbitals, all four electrons occupy the  $t_{2g}$  shell in the  $d^4$  ground state as well as in the lowest excited states with  $d^3$  and  $d^5$  multiplets. For the assignment of peaks A and B at 1 eV and 2 eV, it is sufficient to consider the Coulomb interaction within the  $t_{2g}$  shell, which can be described by two parameters, the intra-orbital Coulomb repulsion  $U$  and Hund coupling  $J_H$  [67, 68]. In cubic approximation, the  $d^4$  ground state is given by the  $S=1$  multiplet  $^3T_1$  at  $6U - 13J_H$ , see Tab. I. At this stage, we may neglect tetragonal distortion and spin-orbit coupling, which will be considered below for the quantitative analysis.

The Mott-Hubbard excitation energies of the different  $|d_i^3, d_j^5\rangle$  excited states are given by

$$\begin{aligned} E_{\text{MH},m} &= E(t_{2g}^3(m)) + E(t_{2g}^5(^2T_2)) - 2E(t_{2g}^4(^3T_1)) \\ &= E(t_{2g}^3(m)) - 2U + 6J_H. \end{aligned} \quad (1)$$

Since all six  $t_{2g}^5$  configurations belong to the same cubic  $^2T_2$  multiplet, the excitation energies  $E_{\text{MH},m}$  are determined by the four  $t_{2g}^3$  multiplets  $^4A_2$ ,  $^2T_1$ ,  $^2E$ , and  $^2T_2$ . Since  $^2T_1$  and  $^2E$  are degenerate, there are only three different values of  $E_{\text{MH},m}$ , see Tab. I.

In cubic approximation, peaks A and B hence correspond to excitations to  $|d_i^3(^4A_2), d_j^5(^2T_2)\rangle$  and  $|d_i^3(^2T_1/2E), d_j^5(^2T_2)\rangle$ , respectively. This assignment is supported by LDA+DMFT calculations [28] which obtain good agreement with other experimental results for two different parameter sets, either  $U=2.3$  eV and  $J_H=0.4$  eV or  $U=3.1$  eV and  $J_H=0.7$  eV. The former set yields 1.1 eV and 2.3 eV for peaks A and B in  $\sigma_1(\omega)$ , in good agreement with our data. We neglect the  $t_{2g}^3(^2T_2)$  multiplet since the corresponding excitation energy  $U + 2J_H$  lies above 3 eV, the absorption band hence overlaps with charge-transfer excitations. In  $\text{Ca}_2\text{RuO}_4$ , the applicability of the local multiplet picture is further supported by ARPES [42], where the electron removal states closest to the Fermi energy  $E_F$  have been found to show  $t_{2g}^3$  character. At 150 K, ARPES finds two flat bands at 0.8 eV and 1.7 eV below  $E_F$  [42]. The former has been attributed to the  $^4A_2$  multiplet, and the energy difference of 0.9 eV between the  $t_{2g}^3$  ARPES bands agrees with the splitting between peaks A and B in our optical data, in agreement with Eq. 1. The flatness

multiplet	energy [28]	$E_{\text{MH},m}$
$t_{2g}^4(^3T_1)$	$6U - 13J_H$	
$t_{2g}^5(^2T_2)$	$10U - 20J_H$	
$t_{2g}^3(^4A_2)$	$3U - 9J_H$	$U - 3J_H$
$t_{2g}^3(^2T_1/2E)$	$3U - 6J_H$	$U$
$t_{2g}^3(^2T_2)$	$3U - 4J_H$	$U + 2J_H$

TABLE I. Cubic multiplets relevant for peaks A and B and their energies in terms of the intra-orbital Coulomb repulsion  $U$  and Hund coupling  $J_H$  [28, 68, 69]. The third column gives the corresponding Mott-Hubbard excitation energy, see Eq. (1).

of the ARPES bands explains the observation of well-defined peaks in  $\sigma_1(\omega)$ . For the band at 1.7 eV below  $E_F$ , the flat character was attributed to the strong anisotropy in spin space and the quasi-1D character of  $xz/yz$  bands [43].

A third ARPES band lying about 2 eV below  $E_F$  has been attributed to the  $^2E$  multiplet [42]. It exhibits a larger dispersion, suggesting the existence of a broad feature at about 2.5 eV in  $\sigma_1(\omega)$ . However, our theoretical analysis below shows that the  $^2E$  multiplet carries much less spectral weight in  $\sigma_1(\omega)$  than the  $^2T_1$  multiplet. The weakness and large width explain the absence of a clear feature in our data.

Our peak assignment further agrees with the results of Jung *et al.* [34], who combined optical spectroscopy with an LDA+ $U$  study neglecting spin-orbit coupling (see also [35]). A different assignment was favored by Lee *et al.* [63] but they neglect rotation and tilt of the octahedra. In this case, the matrix elements for peak A vanish. We will address the spectral weight and in particular the effect of spin-orbit coupling in Sect. VI.

## V. TETRAGONAL CRYSTAL FIELD

The energy difference  $\hbar\Delta\omega$  between peaks A and B increases from 0.9 eV at 15 K to 1.1 eV at 300 K, see Fig. 3. In cubic approximation, one expects a temperature-independent value,  $\hbar\Delta\omega=3J_H$ . The experimental result can be rationalized by taking into account the temperature-dependent distortion of the  $\text{RuO}_6$  octahedra [21]. The tetragonal crystal field lowers the  $xy$  orbital by  $\Delta_{\text{CF}}$  with respect to  $xz$  and  $yz$  and lifts the degeneracy of the  $t_{2g}^4(^3T_1)$  multiplet. This yields  $xy$  orbital order, the local  $d^4$  ground state being the spin triplet  $|xy^2, S_z\rangle$  (spin  $S=1$ ,  $S_z=\pm 1, 0$ ) with double occupancy of the  $xy$  orbital [28],

$$\begin{aligned} |xy^2, 1\rangle &= c_{xz\uparrow}^\dagger c_{yz\uparrow}^\dagger c_{xy\uparrow}^\dagger c_{xy\downarrow}^\dagger |0\rangle \\ |xy^2, 0\rangle &= \frac{1}{\sqrt{2}} \left( c_{xz\uparrow}^\dagger c_{yz\downarrow}^\dagger + c_{xz\downarrow}^\dagger c_{yz\uparrow}^\dagger \right) c_{xy\uparrow}^\dagger c_{xy\downarrow}^\dagger |0\rangle \\ |xy^2, -1\rangle &= c_{xz\downarrow}^\dagger c_{yz\downarrow}^\dagger c_{xy\uparrow}^\dagger c_{xy\downarrow}^\dagger |0\rangle, \end{aligned} \quad (2)$$

where  $|0\rangle$  denotes the vacuum state and  $c_{\tau\sigma}^\dagger$  creates an electron in orbital  $\tau$  with spin  $\sigma$ .

The tetragonal field also splits the  $t_{2g}^5(^2T_2)$  multiplet but this does not yield a splitting in  $\sigma_1(\omega)$  since adding an electron to  $|xy^2, S_z\rangle$  only yields those  $t_{2g}^5$  states with doubly occupied

$xy$  orbital. All of them have the same energy. Considering the  $d^3$  states, the  $^4A_2$  and  $^2E$  multiplets are not split by a tetragonal field but  $^2T_1$  is. The three lowest Mott-Hubbard excitation energies then are

$$E_A = U - 3J_H + \Delta_{\text{CF}} \quad (3)$$

$$E_B = U + \Delta_{\text{CF}} + J_H - \sqrt{\Delta_{\text{CF}}^2 + J_H^2} \quad (4)$$

$$E_C = U + \Delta_{\text{CF}}. \quad (5)$$

Since  $U$  and  $J_H$  can be viewed as being independent of temperature, this yields several ways to estimate  $\Delta_{\text{CF}}(T)$ . From Eq. (3) we obtain

$$\Delta_{\text{CF}}(T) = \Delta_{\text{CF}}(15 \text{ K}) + \hbar\omega_A(T) - \hbar\omega_A(15 \text{ K}), \quad (6)$$

which is plotted in Fig. 5 for  $\Delta_{\text{CF}}(15 \text{ K}) \approx 0.34 \text{ eV}$  as determined from the peak energy observed in RIXS [44, 66]. The RIXS peak directly yields  $\Delta_{\text{CF}}$  if we assume  $\zeta = 0$ . For finite  $\zeta$ , the excitation energy is slightly larger than  $\Delta_{\text{CF}}$ , see Fig. 1. Below we establish  $\Delta_{\text{CF}}/\zeta \geq 2.4$  as a lower bound, in which case the average excitation energy amounts to  $\lesssim 1.1 \Delta_{\text{CF}}$ .

The RIXS data show little change between 16 K and 125 K [66], in agreement with our result. Additionally, we find that  $\Delta_{\text{CF}}$  is strongly suppressed at 300 K, in agreement with the strongly reduced distortion of the  $\text{RuO}_6$  octahedra that changes from compression to elongation at about 300 K [21, 25]. The strong suppression of  $\Delta_{\text{CF}}$  also agrees with the pronounced change of the orbital occupation observed in x-ray absorption [37, 70]. Furthermore, resonant elastic scattering suggests that the orbital polarization vanishes close to 300 K [71]. Note, however, that undistorted octahedra do not imply that  $\Delta_{\text{CF}}(300 \text{ K})$  vanishes exactly because we also have to consider the crystal-field contributions of further neighbors in the layered crystal structure.

For a second estimate, we identify the experimental peak splitting  $\Delta\omega = \omega_B - \omega_A$  with  $E_B - E_A$  and find

$$\Delta_{\text{CF}}^2(T) = \left[ \sqrt{\Delta_{\text{CF}}^2(15 \text{ K}) + J_H^2} + \hbar\Delta\omega(15 \text{ K}) - \hbar\Delta\omega(T) \right]^2 - J_H^2. \quad (7)$$

The result agrees well with that of Eq. (6) for  $J_H = 0.35 \text{ eV}$ , see open symbols in Fig. 5. First-principles calculations [28] find  $\Delta_{\text{CF}} \approx 0.3 \text{ eV}$  in the insulating phase at 180 K and 0.1 eV in the metallic phase at 400 K. Considering spin-orbit coupling and further on-site  $4d^4$  excitation energies,  $L$  edge RIXS results yield  $\Delta_{\text{CF}} = 0.25 \text{ eV}$  and  $\zeta = 0.13 \text{ eV}$  at 12 K [44].

## VI. SPECTRAL WEIGHT AND SPIN-ORBIT COUPLING

Spin-orbit coupling  $\zeta = 2\lambda$  is of the order of 0.1 eV in  $\text{Ca}_2\text{RuO}_4$  [28, 44] and thus can be neglected for the assignment of broad peaks observed at 1 eV and 2 eV. However, it plays a decisive role for the spectral weight of these peaks since it affects the orbital occupation, lifting the degeneracy of the  $|xy^2, S_z\rangle$  ground state. In the following, we first calculate the spectral weight for a finite tetragonal crystal-field splitting  $\Delta_{\text{CF}}$  with  $\zeta = 0$ . In a second step, we study finite  $\zeta$ .

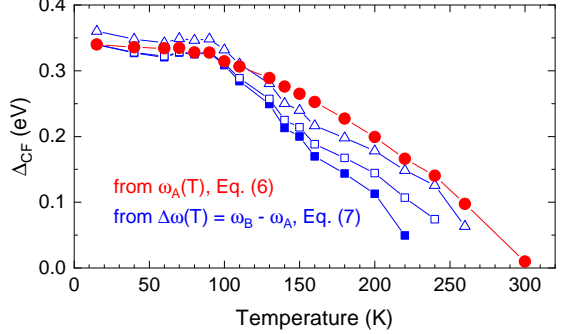


FIG. 5. Tetragonal crystal-field splitting  $\Delta_{\text{CF}}(T)$  based on Eq. (6) (red) for  $\Delta_{\text{CF}}(15 \text{ K}) = 0.34 \text{ eV}$  [44, 66]. Blue symbols denote the result of Eq. (7) for  $J_H = 0.4 \text{ eV}$  (full) or  $0.35 \text{ eV}$  (open) with  $\Delta_{\text{CF}}(15 \text{ K}) = 0.34 \text{ eV}$  (squares) or  $0.36 \text{ eV}$  (triangles).

### 1. Double occupancy of $xy$ for $\zeta = 0$

The optical matrix elements for Mott-Hubbard excitations depend on the hopping amplitudes between nearest-neighbor Ru sites and hence reflect spin and orbital correlations, see Appendix B. The restriction to nearest-neighbor sites is justified since hopping to further neighbors is small. In our optical data, we could not resolve any anisotropy within the  $ab$  plane. We therefore treat all nearest-neighbor Ru-Ru pairs as equivalent and consider a Ru-O-Ru bond along the global  $x$  axis. On each of the two Ru sites  $k \in \{i, j\}$ , we employ a local reference frame  $(x_k, y_k, z_k)$  where the local axes point from the central Ru ion towards the O ligands. The effective Ru-Ru hopping matrix from  $(xy_i, yz_i, xz_i)$  to  $(xy_j, yz_j, xz_j)$  reads

$$\hat{t} = \frac{t_{pd\pi}^2}{\Delta_{\text{CT}}} \begin{pmatrix} \alpha_{xy} & 0 & -\beta \\ 0 & 0 & 0 \\ \beta & 0 & \alpha_{xz} \end{pmatrix}, \quad (8)$$

where  $t_{pd\pi}$  denotes Ru-O hopping and  $\Delta_{\text{CT}}$  is the charge transfer energy. Using the local reference frames has the advantage to yield zero hopping for all processes that involve  $yz_k$  orbitals. The coefficients  $\alpha_u$  and  $\beta$  depend on the octahedral tilt and rotation angles  $\theta$  and  $\varphi$  which are taken into account by a rotation on the O ion from one reference frame to the other. For a  $180^\circ$  bond one obtains  $\alpha_{xy} = \alpha_{xz} = 1$  and  $\beta = 0$ . In  $\text{Ca}_2\text{RuO}_4$ , both  $\theta$  and  $\varphi$  roughly equal  $11^\circ$  and show only a small change as a function of temperature [9]. This yields  $\alpha_{xy} \approx 0.88$ ,  $\alpha_{xz} \approx 0.95$ , and  $\beta \approx 0.31$ . For simplicity, we employ  $\alpha_{xy} = \alpha_{xz} = 1$  and  $\beta = 1/3$ .

For double occupancy of the  $xy$  orbital and AF order, the hopping matrix yields the optical matrix elements

$$|M(^4A_2)|^2 = \frac{2}{3}\beta^2 \left( t_{pd\pi}^2 / \Delta_{\text{CT}} \right)^2 \quad (9)$$

$$|M(^2T_1)|^2 = \left( t_{pd\pi}^2 / \Delta_{\text{CT}} \right)^2 \quad (10)$$

$$|M(^2E)|^2 = \frac{4}{3}\beta^2 \left( t_{pd\pi}^2 / \Delta_{\text{CT}} \right)^2 \quad (11)$$

where we neglect the small spin canting of about  $3.5^\circ$  [25] and treat spins on neighboring sites as being antiparallel. The

spectral weight of the  $^2E$  multiplet vanishes in the absence of octahedral tilt and rotation, i.e.,  $\beta=0$ . Therefore, its contribution to  $\sigma_1(\omega)$  is about an order of magnitude smaller than the one of the  $^2T_1$  multiplet. This may explain why we cannot resolve a weak separate contribution of the  $^2E$  states, in contrast to ARPES [42].

The spectral weight of the  $^4A_2$  multiplet, which corresponds to peak A in  $\sigma_1(\omega)$ , also vanishes for  $\beta=0$ . For comparison with experiment, we are mainly interested in the spectral weight ratio  $SW_A/SW_B$ . For  $\beta=1/3$  and AF order at  $T=0$ , Eqs. (9) and (10) predict  $SW_A/SW_B = \frac{2}{3}\beta^2 \omega_B/\omega_A \approx 0.13$ , in clear disagreement with the experimental result 1/3 to 1/4. This discrepancy can be resolved by considering finite spin-orbit coupling  $\zeta$ , as discussed below.

The spectral weight reflects nearest-neighbor spin and orbital correlations. In the limit  $\zeta=0$  with  $\Delta_{CF} > 0$ , the local ground state is given by Eq. (2) and the orbital occupation is independent of the size of  $\Delta_{CF}$ . In this limit, the temperature dependence of the spectral weight reflects changes of the nearest-neighbor spin-spin correlations. In layered  $\text{Ca}_2\text{Ru}_{0.99}\text{Ti}_{0.01}\text{O}_4$ , we do not expect pronounced changes of the spectral weight at  $T_N$ . In two-dimensional materials, the spin correlation length remains large above the three-dimensional ordering temperature, and both the correlation length and the nearest-neighbor spin-spin correlations drop slowly with increasing temperature. The corresponding slow change of the spectral weight was observed in the layered  $3d^4$  compound  $\text{LaSrMnO}_4$  [53]. Without a detailed theoretical prediction for the behavior of the spin-spin correlations, we have to compare the results for the AF ordered state at  $T=0$  given in Eqs. (9) and (10) with those for a magnetically fully disordered state at  $T \gg T_N$ , neglecting any change of the orbital occupation. We emphasize that the octahedral tilt and rotation angles and hence  $\beta$  do not vary strongly with temperature [9]. For the  $^4A_2$  multiplet we find an increase of spectral weight by a factor 2, similar to our experimental result for peak A. However,  $^2T_1$  and  $^2E$  exhibit the opposite behavior, a suppression by a factor 2, in contrast to the optical data, see inset of Fig. 2a and Fig. 3. Our predictions roughly agree with LDA+ $U$  results for peaks A and B which also neglect spin-orbit coupling [34, 35]. Such opposite behavior of the lowest two absorption bands indeed was observed in the  $3d^2$  compound  $\text{YVO}_3$  [57], an electron analogue to the  $d^4$  configuration but with the three-dimensional perovskite structure. Note that spin-orbit coupling is negligible for the  $3d$  vanadates. We conclude that neither the experimental value of  $SW_A/SW_B$  at 15 K nor the temperature dependence of  $SW_B$  can be described in a scenario that neglects spin-orbit coupling.

## 2. Finite spin-orbit coupling

Spin-orbit coupling affects the orbital occupation and hence the spectral weights. In the following, we first discuss the effect of finite  $\zeta$  on the electronic states and then address the spectral weight as a function of  $\Delta_{CF}/\zeta$ .

In the limit  $\Delta_{CF}=0$ , i.e., cubic symmetry, the  $^3T_1$  ground state shows spin  $S=1$  and  $L_{\text{eff}}=1$ . These are coupled to

$J=0, 1$ , and  $2$ , and the corresponding states have the energies  $-\zeta$ ,  $-\zeta/2$ , and  $+\zeta/2$ , respectively, see Fig. 1. In the opposite limit,  $\zeta=0$  and positive  $\Delta_{CF}$ , the ground state is a spin triplet with double occupancy of the  $xy$  orbital, cf. Eq. (2). In between these two limits, the local ground state for a single  $d^4$  site is given by the singlet  $|s\rangle$  [26, 72],

$$|s\rangle = \cos \theta_s |xy^2, 0\rangle \quad (12)$$

$$+ \frac{\sin \theta_s}{2} (-|yz^2, 1\rangle + |yz^2, -1\rangle + i|xz^2, 1\rangle + i|xz^2, -1\rangle)$$

and the lowest excited state is the doublet  $|d_{\pm 1}\rangle$ ,

$$|d_{+1}\rangle = \cos \theta_d |xy^2, 1\rangle + \frac{\sin \theta_d}{\sqrt{2}} (i|xz^2, 0\rangle + |yz^2, 0\rangle) \quad (13)$$

$$|d_{-1}\rangle = \cos \theta_d |xy^2, -1\rangle + \frac{\sin \theta_d}{\sqrt{2}} (i|xz^2, 0\rangle - |yz^2, 0\rangle) \quad (14)$$

where the prefactors depend only on  $\Delta_{CF}/\zeta$  [26],

$$\tan \theta_d = \left( (\Delta_{CF}/\zeta) + \sqrt{1 + (\Delta_{CF}/\zeta)^2} \right)^{-1}$$

$$\tan \theta_s = \sqrt{1 + \gamma^2} - \gamma \quad \text{for } \gamma = ((\Delta_{CF}/\zeta) - 1/2) / \sqrt{2}.$$

For  $\zeta=0$  one finds  $\cos \theta_s = \cos \theta_d = 1$ , which yields the states  $|xy^2, S_z\rangle$  described in Eq. (2). The other states  $|yz^2, S_z\rangle$  and  $|xz^2, S_z\rangle$  correspond to double occupancy of the  $yz$  or  $xz$  orbital, respectively, and are constructed equivalently, cf. Eq. (2) [28]. The ratio  $\Delta_{CF}/\zeta$  determines the orbital occupation and thereby strongly affects the spectral weight.

The energies of singlet and doublet are given by

$$E_s/(\zeta/2) = -\frac{\Delta_{CF}}{3\zeta} - \frac{1}{2} - \sqrt{\left(\frac{\Delta_{CF}}{\zeta} - \frac{1}{2}\right)^2 + 2} \quad (15)$$

$$E_d/(\zeta/2) = -\frac{\Delta_{CF}}{3\zeta} - \sqrt{\left(\frac{\Delta_{CF}}{\zeta}\right)^2 + 1} \quad (16)$$

and their splitting amounts to  $E_{sd} \approx (\zeta/2)^2/\Delta_{CF}$  in the limit  $\zeta \ll \Delta_{CF}$ . The local non-magnetic singlet ground state obtained for any finite value of  $\zeta$  appears to be at odds with the occurrence of magnetic order below  $T_N$ . Starting from this single-site singlet picture, however, van-Vleck-type magnetism can be favored on the lattice by exchange interactions between excited states [22]. Antiferromagnetic order with magnetic moments pointing within the  $ab$  plane, as observed experimentally, is achieved via condensation of [23, 32, 33]

$$|d_{x/y}\rangle = \frac{1}{\sqrt{2}} (|d_{+1}\rangle \pm |d_{-1}\rangle), \quad (17)$$

where the  $+$  ( $-$ ) sign refers to  $|d_x\rangle$  ( $|d_y\rangle$ ). The actual local ground state is a mixture of  $|d_{x/y}\rangle$  and singlet  $|s\rangle$  which in particular depends on hopping interactions [32, 33]. A determination of the precise ground state on the lattice is beyond the scope of our study but it turns out that this is not necessary to obtain a reliable estimate of  $\Delta_{CF}/\zeta$ . First of all we find the lower bound  $\Delta_{CF}/\zeta > 2.2 \pm 0.3$  if we neglect any singlet

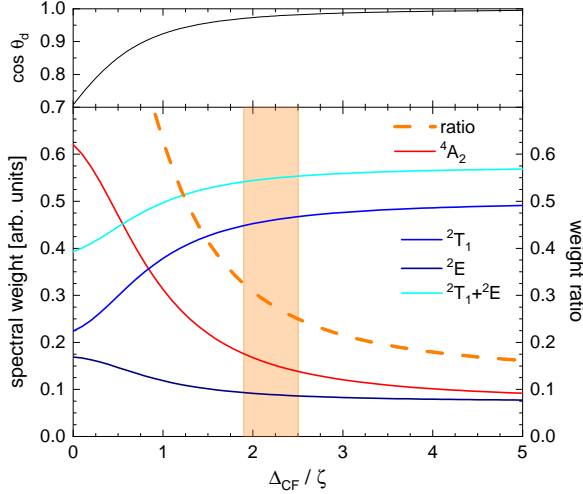


FIG. 6. Results for the doublet ground state  $|d_{+1}\rangle_i|d_{-1}\rangle_j$  which neglects any singlet contribution. Top: Weight factor  $\cos \theta_d$  for double occupancy of the  $xy$  orbital, cf. Eqs. (13) and (14). Bottom, left axis: Spectral weight of peak A ( $^4A_2$  multiplet, red) and of the two contributions to peak B ( $^2T_1$  and  $^2E$ , blue) as a function of  $\Delta_{CF}/\zeta$ . Right axis (dashed orange line): spectral weight ratio  $SWR = SW(^4A_2)/SW(^2T_1 + ^2E)$ . The shaded area denotes the range  $1/4 \leq SWR \leq 1/3$ .

contribution and consider  $|d_{+1}\rangle_i|d_{-1}\rangle_j$  as ground state for the calculation of the optical spectral weight. Using the abbreviations  $c_\theta = \cos \theta_d$  and  $s_\theta = \sin \theta_d$ , we find the matrix elements

$$|M_{d_{\pm 1}}(^4A_2)|^2 = \left[ \frac{2}{3} \beta^2 c_\theta^4 + 2 c_\theta^2 s_\theta^2 + \frac{1+2\beta^2}{3} s_\theta^4 \right] \frac{t_{pd\pi}^4}{\Delta_{CT}^2}$$

$$|M_{d_{\pm 1}}(^2T_1)|^2 = \left[ c_\theta^4 + \beta^2 c_\theta^2 s_\theta^2 + \frac{5+4\beta^2}{8} s_\theta^4 \right] \frac{t_{pd\pi}^4}{\Delta_{CT}^2}$$

$$|M_{d_{\pm 1}}(^2E)|^2 = \left[ \frac{4}{3} \beta^2 c_\theta^4 + c_\theta^2 s_\theta^2 + \frac{1+2\beta^2}{6} s_\theta^4 \right] \frac{t_{pd\pi}^4}{\Delta_{CT}^2}.$$

The corresponding spectral weights are plotted as a function of  $\Delta_{CF}/\zeta$  for  $\beta = 1/3$  in Fig. 6, which also shows the behavior of  $\cos \theta_d$ . The spectral weight of the  $^4A_2$  multiplet (red), which corresponds to peak A, is boosted by spin-orbit coupling. This directly reflects the dependence of the ground state wavefunction on  $\Delta_{CF}/\zeta$ . A decrease of  $\Delta_{CF}/\zeta$  yields an enhanced admixture of  $|xz^2, 0\rangle$  to  $|d_{\pm 1}\rangle$ , see Eqs. (13) and (14). The doubly occupied  $xz$  orbital allows for contributions to peak A via diagonal hopping processes from  $xz_i$  to  $xz_j$  or from  $xy_i$  to  $xy_j$ . In the spectral weight, their prefactor  $\alpha^2 = 1$  is larger than  $\beta^2 = 1/9$  for the off-diagonal contributions, see Eq. (8). In contrast, the spectral weights of the  $^2T_1$  and  $^2E$  multiplets do not vary strongly for  $\Delta_{CF}/\zeta \gtrsim 1.5$ .

Our calculations reveal a strong dependence of the ratio  $SW(^4A_2)/SW(^2T_1 + ^2E)$  on  $\Delta_{CF}/\zeta$  (dashed orange), which allows us to estimate this important parameter. The shaded area in Fig. 6 indicates the range in which the calculation agrees with the experimental result  $SW_A/SW_B = 1/3$  to  $1/4$ .

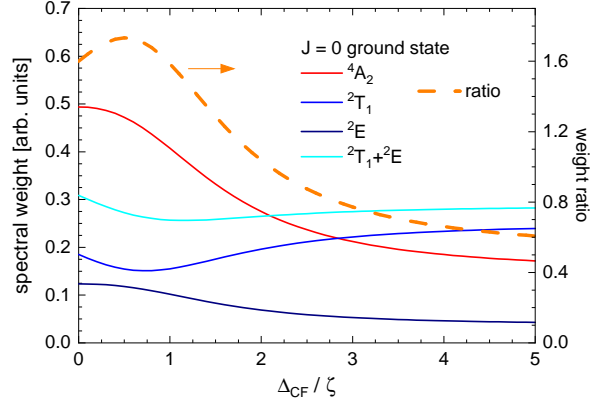


FIG. 7. Results for the singlet ground state  $|s\rangle_i|s\rangle_j$ . Left axis: Spectral weight of peak A ( $^4A_2$  multiplet, red) and of the two contributions to peak B ( $^2T_1$  and  $^2E$ , blue). Right axis (dashed orange line): The spectral weight ratio  $SW(^4A_2)/SW(^2T_1 + ^2E)$  is much larger than for the doublet ground state considered in Fig. 6.

For the chosen hypothetical ground state  $|d_{+1}\rangle_i|d_{-1}\rangle_j$  this yields  $\Delta_{CF}/\zeta = 2.2 \pm 0.3$ , which agrees with a recent analysis of RIXS data [44]. However, our result denotes a lower limit of  $\Delta_{CF}/\zeta$  since it neglects contributions of the singlet. We find that adding a finite singlet weight to  $|d_{+1}\rangle_i|d_{-1}\rangle_j$  raises the result for  $\Delta_{CF}/\zeta$ . To illustrate this, we plot the spectral weights for the two-site singlet ground state  $|s\rangle_i|s\rangle_j$  in Fig. 7. For  $\Delta_{CF}/\zeta \gtrsim 1$ , the spectral weight of  $^4A_2$  is strongly enhanced while that of  $^2T_1 + ^2E$  is strongly reduced compared to the doublet-type ground state. The much larger spectral weight ratio exceeds the experimental value  $1/3$  to  $1/4$  for any  $\Delta_{CF}/\zeta$ .

For a more realistic scenario, we have to take into account that the moments in  $\text{Ca}_2\text{RuO}_4$  are lying within the  $ab$  plane in the ordered phase. This requires to consider the superposition of  $|d_x\rangle$  (or equivalently  $|d_y\rangle$ ) with the singlet [23, 32, 33],

$$|g_x\rangle = (\sin \Phi |s\rangle_i + \cos \Phi |d_x\rangle_i) \\ \cdot (\sin \Phi |s\rangle_j - \cos \Phi |d_x\rangle_j) \quad (18)$$

where  $|s\rangle$  and  $|d_x\rangle$  depend on  $\Delta_{CF}/\zeta$ , see Eqs. (12) – (14) and (17), and  $0 \leq \Phi \leq \pi$ . The  $+/$  – signs denote the relative phases between  $\sin \Phi |s\rangle$  and  $\cos \Phi |d_x\rangle$  for which we obtain the lower bound of  $\Delta_{CF}/\zeta$  for this type of ground state. For each  $\Phi$  we calculate the spectral weights. As an example, Fig. 8 plots the curves for equal weights of singlet and doublet,  $\sin^2(\Phi) = 1/2$ . This yields the range of  $\Delta_{CF}/\zeta$  in which the calculated spectral weight ratio agrees with the experimental result  $1/3$  to  $1/4$  at 15 K, see orange shaded range in Figs. 8 and 9. The grey shaded range shows the corresponding solution for  $|g_y\rangle$  which differs from the result for  $|g_x\rangle$  since we consider a bond parallel to  $x$ . Experimentally, we could not resolve any in-plane anisotropy, hence our data correspond to an average over both cases. For this realistic ground state, we find a lower bound  $\Delta_{CF}/\zeta \geq 2.4$  that is reached for singlet weight  $\sin^2(\Phi)$  in the vicinity of  $1/2$ . Note that a variational cluster approach indeed points towards similar weights of singlet and doublet for parameters applicable to the case of

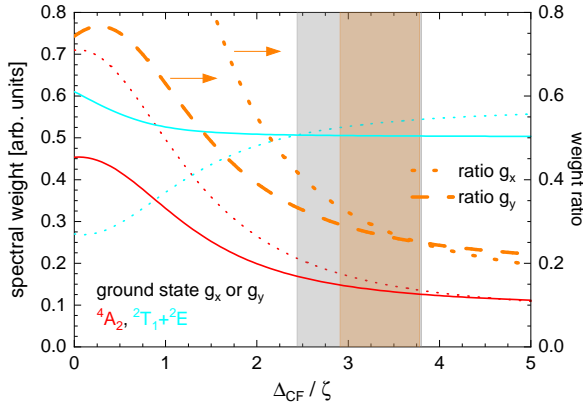


FIG. 8. Spectral weights for the realistic ground states  $|g_x\rangle$  (dotted) and  $|g_y\rangle$  (solid lines) for  $\sin^2(\Phi) = 1/2$ , see Eq. (18). Data for  $^4A_2$  (red) and  $^2T_1 + ^2E$  (cyan) correspond to peaks A and B, respectively. Orange curves depict their ratio  $SWR$  (right axis), and the shaded range gives the values of  $\Delta_{CF}/\zeta$  for which  $1/4 \leq SWR \leq 1/3$  (orange for  $|g_x\rangle$ , grey for  $|g_y\rangle$ ; cf. Fig. 9).

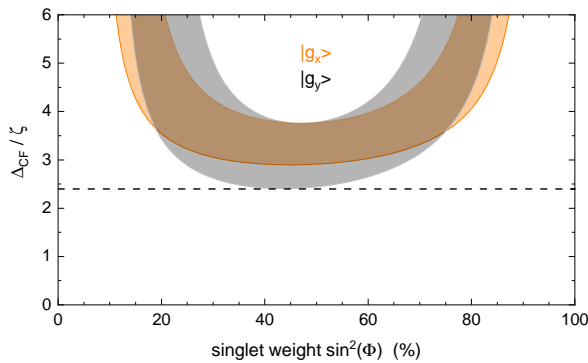


FIG. 9. Results for the realistic ground states  $|g_x\rangle$  (orange, Eq. 18), and  $|g_y\rangle$  (grey). The shaded range depicts the values of  $\Delta_{CF}/\zeta$  for which the calculated spectral weight ratio  $SW(^4A_2)/SW(^2T_1 + ^2E)$  lies within the experimental result  $1/3$  to  $1/4$ . The dashed line highlights the lower limit  $\Delta_{CF}/\zeta \geq 2.4$ .

$\text{Ca}_2\text{RuO}_4$  [32].

To estimate the upper bound of  $\Delta_{CF}/\zeta$ , we use the RIXS peak frequency 0.34 eV [44, 66] as the upper limit of  $\Delta_{CF}$ , see Fig. 1. For  $\zeta$ , different values were claimed, e.g., 0.11 eV [29], 0.13 eV [44], or 0.4 eV [65]. As a lower limit, we use  $\zeta = 0.08$  eV which was found in an analysis of inelastic neutron data [30] and was also used to analyze RIXS data of  $\text{Ca}_2\text{RuO}_4$  [66]. This yields  $\Delta_{CF}/\zeta \lesssim 4$ . Altogether, our final result hence reads  $2.4 \leq \Delta_{CF}/\zeta \lesssim 4$ . In this parameter range, we deduce  $0.31 \text{ eV} \lesssim \Delta_{CF} \lesssim 0.34 \text{ eV}$  by identifying the RIXS peak at 0.34 eV [44, 66] with the average excitation energy plotted in the right panel of Fig. 1, which finally yields  $0.08 \text{ eV} \lesssim \zeta \lesssim 0.14 \text{ eV}$ . Our findings agree very well with LDA+DMFT calculations that find  $\Delta_{CF} = 0.32$  eV,  $\zeta = 0.106$  eV, and hence  $\Delta_{CF}/\zeta \approx 3$ . According to different theoretical approaches, these parameters are safely in the range of AF order with moments lying in the  $ab$  plane [31, 33].

### 3. Temperature dependence

In  $\text{Ca}_2\text{RuO}_4$ , also the behavior at finite temperature is characterized by the competition between spin-orbit coupling and crystal field [74]. In general, the temperature dependence of the spectral weight reflects the behavior of nearest-neighbor spin and orbital correlations. Due to the prominent role of  $\zeta$ , these need to be addressed simultaneously in  $\text{Ca}_2\text{RuO}_4$ . Without more detailed knowledge on the precise  $T = 0$  ground state on the lattice, we do not attempt to quantitatively address the temperature dependence for finite  $\zeta$ . Qualitatively, however, the experimental data can be explained by the pronounced temperature dependence of  $\Delta_{CF}$ . With increasing temperature, the decrease of  $\Delta_{CF}/\zeta$  yields a pronounced increase of peak A. This occurs in all the examples that we studied, see Figs. 6 – 8. For peak B, our experimental data show an increase of spectral weight with increasing temperature, i.e., decreasing  $\Delta_{CF}/\zeta$ . This trend is reproduced for the realistic ground state  $|g_y\rangle$ , see Fig. 8.

## VII. CONCLUSION

In the layered ruthenates  $\text{Ca}_{2-x}\text{Sr}_x\text{RuO}_4$ , the competition of spin-orbit coupling  $\zeta = 2\lambda$  and crystal-field splitting  $\Delta_{CF}$  has been discussed controversially over many years. We have shown that the optical spectral weight of Mott-Hubbard excitations in  $4d^4$  compounds is a direct measure of the central parameter  $\Delta_{CF}/\zeta$ . The sensitivity of the optical data is based on the pronounced effect that  $\Delta_{CF}/\zeta$  has on the ground state wavefunction. The optical matrix elements reflect the orbital occupation which strongly depends on  $\Delta_{CF}/\zeta$ . This is different from the limiting cases  $\Delta_{CF} = 0$  or  $\zeta = 0$ , where the ground state is insensitive to the size of the finite one of the two parameters, at least over large ranges. In  $3d$  transition-metal compounds with negligible spin-orbit coupling, the spectral weight of Mott-Hubbard excitations reflects nearest-neighbor spin and orbital correlations but it does not directly allow to determine the size of the crystal field. This rather requires to consider the excitation energies. The possibility to determine  $\Delta_{CF}/\zeta$  directly from the spectral weight in compounds with sizable spin-orbit coupling such as the  $4d^4$  ruthenates is the central result of this study.

In  $\text{Ca}_{2-x}\text{Sr}_x\text{RuO}_4$ , we have focused on the lowest Mott-Hubbard excitations at about 1 eV and 2 eV in the optical conductivity. Based on the excitation energies, we observe a pronounced temperature dependence of  $\Delta_{CF}$ , as expected from the behavior of the octahedral distortion. In particular we find that  $\Delta_{CF}$  is strongly suppressed at room temperature. At low temperature, the optical spectral weight allows us to estimate a lower bound  $\Delta_{CF}/\zeta \geq 2.4$  which is reached for a ground state with roughly similar weights of singlet and doublet. Altogether we find  $0.31 \text{ eV} \lesssim \Delta_{CF} \lesssim 0.34 \text{ eV}$  and  $0.08 \text{ eV} \lesssim \zeta \lesssim 0.14 \text{ eV}$ .

On the one hand, one may conclude that  $\text{Ca}_2\text{RuO}_4$  is firmly rooted in the range of dominant crystal field. For instance the energy scales of the lowest excitations are not given by  $\zeta$  but rather by  $(\zeta/2)^2/\Delta_{CF}$  and  $\Delta_{CF}$ . On the other hand, spin-

orbit coupling still plays a most important role in  $\text{Ca}_2\text{RuO}_4$ . For the low-energy magnetic excitations, spin-orbit coupling may be treated perturbatively but it gives rise to an unusually strong anisotropy. Considering electronic excitations such as predominantly local crystal-field-type excitations or intersite Mott-Hubbard excitations, the matrix elements are strongly affected by spin-orbit coupling and the local non-magnetic singlet ground state poses a challenge for quantitative calculations. In the end, the captivating character of  $\text{Ca}_2\text{RuO}_4$  is based on the *competition* of spin-orbit coupling and crystal field rather than on the dominance of one of them.

## ACKNOWLEDGEMENT

We acknowledge funding from the Deutsche Forschungsgemeinschaft (DFG, German Research Foundation) – Project No. 277146847 – CRC 1238 (Projects A02, B02, and C02). M.H. is supported by the Knut and Alice Wallenberg Foundation as part of the Wallenberg Academy Fellows project.

## APPENDIX

### A. Anisotropy

Our analysis focuses on peaks A and B, i.e., Mott-Hubbard excitations that do not contribute to the  $c$ -axis response of  $\text{Ca}_2\text{RuO}_4$  [34]. Their energies provide the basis for Fig. 5, and the spectral weight ratio  $SW_A/SW_B$  at 15 K yields our estimate of  $\Delta_{\text{CF}}/\zeta$ . In the chosen measurement geometry, the pseudo-dielectric function allows us to reliably determine these quantities [64]. This is supported by the good overall agreement of our experimental data with reflectivity-based results [34, 63]. Moreover, this claim is corroborated by an alternative approach which explicitly considers the anisotropy. In this case, we simultaneously analyze our ellipsometric data and  $\sigma_{\parallel c}$ , the optical conductivity for polarization parallel to  $c$  reported by Jung *et al.* [34]. This allows us to determine  $\sigma_{\perp c}$ . Note that the  $c$ -axis data shows little temperature dependence.

In Fig. 10 we compare  $\sigma_{\perp c}$  at 15 K with the data plotted in Fig. 2a. The two curves are very similar. For peaks A and B, we find no effect on the peak energies and minor changes of the spectral weights. For the spectral weight ratio  $SW_A/SW_B$  we find 0.29, in perfect agreement with the values 0.30 and 0.27 discussed in the main text, see Fig. 4.

### B. Optical matrix elements

To calculate the contribution of Mott-Hubbard excitations to the optical conductivity  $\sigma_1(\omega)$ , we consider hopping between nearest-neighbor Ru sites  $i$  and  $j$  at a distance  $d_{\text{Ru}}$  and polarization parallel to this Ru-Ru bond,

$$\sigma_1(\omega) = \frac{d_{\text{Ru}}^2}{N_{\text{conf}}} \sum_{m,m',n,n'} \frac{|M_{n,n'}^{m,m'}|^2}{E_{\text{MH},m}} \delta(\hbar\omega - E_{\text{MH},m}) \quad (19)$$

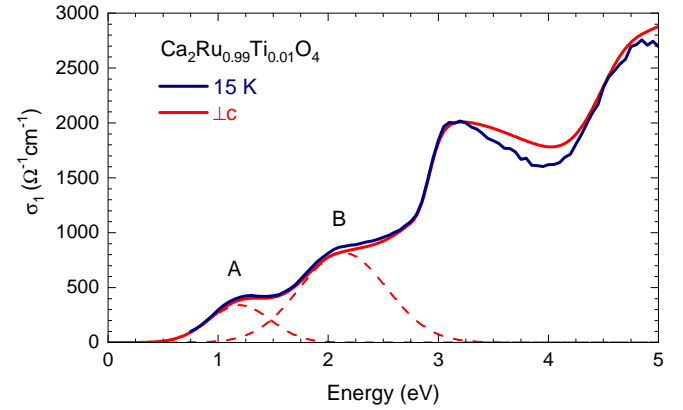


FIG. 10. Taking into account the  $c$ -axis response [34] in a uniaxial model (red) yields a very similar result as the analysis based on the pseudo-dielectric function (blue), cf. Fig. 2a. This applies in particular to peaks A and B (dashed).

where  $m$  and  $m'$  denote the different  $d^3$  and  $d^5$  states, respectively,  $n$  and  $n'$  correspond to the possible  $d^4$  states in the ground state,  $M_{n,n'}^{m,m'}$  is the matrix element,  $E_{\text{MH},m}$  the energy as given in Eq. (1), and  $N_{\text{conf}}$  denotes the number of possible configurations in the ground state. At  $T=0$ , the Néel state shows finite sublattice magnetization, and one finds  $N_{\text{conf}}=2$ . For  $\zeta=0$  and double occupancy of the  $xy$  orbital, the two configurations are  $|xy^2, S_z\rangle_i |xy^2, -S_z\rangle_j$  for  $S_z=\pm 1$ . In this case, the  $S_z=0$  state corresponds to a magnon excitation. For finite  $\zeta$ , the doublet ground state  $|d_{J_z}\rangle_i |d_{-J_z}\rangle_j$  with  $J_z=\pm 1$  also shows  $N_{\text{conf}}=2$ . A magnetically fully disordered state for  $\zeta=0$  and  $\Delta_{\text{CF}}>0$  shows  $N_{\text{conf}}=9$ . The

$c_{xz,\sigma}^\dagger$	$ xy^2, 1\rangle$	$ xy^2, 0\rangle$	$ xy^2, -1\rangle$
$\langle t_{2g}^5(^2T_2, yz \uparrow)  $	$1 (\downarrow)$	$-1/\sqrt{2} (\uparrow)$	$0$
$\langle t_{2g}^5(^2T_2, yz \downarrow)  $	$0$	$1/\sqrt{2} (\downarrow)$	$-1 (\uparrow)$
$c_{xz,\sigma}$	$ xy^2, 1\rangle$	$ xy^2, 0\rangle$	$ xy^2, -1\rangle$
$\langle t_{2g}^3(^2T_1, yz \uparrow)  $	$-1/\sqrt{2} (\uparrow)$	$-1/2 (\downarrow)$	$0$
$\langle t_{2g}^3(^2T_1, yz \downarrow)  $	$0$	$-1/2 (\uparrow)$	$-1/\sqrt{2} (\downarrow)$
$c_{xy,\sigma}$	$ xy^2, 1\rangle$	$ xy^2, 0\rangle$	$ xy^2, -1\rangle$
$\langle t_{2g}^3(^4A_2, 3/2)  $	$-1 (\downarrow)$	$0$	$0$
$\langle t_{2g}^3(^4A_2, -3/2)  $	$0$	$0$	$1 (\uparrow)$
$\langle t_{2g}^3(^4A_2, 1/2)  $	$1/\sqrt{3} (\uparrow)$	$-\sqrt{2/3} (\downarrow)$	$0$
$\langle t_{2g}^3(^4A_2, -1/2)  $	$0$	$\sqrt{2/3} (\uparrow)$	$-1/\sqrt{3} (\downarrow)$
$\langle t_{2g}^3(^2E, a \uparrow)  $	$-\sqrt{2/3} (\uparrow)$	$-1/\sqrt{3} (\downarrow)$	$0$
$\langle t_{2g}^3(^2E, a \downarrow)  $	$0$	$1/\sqrt{3} (\uparrow)$	$\sqrt{2/3} (\downarrow)$

TABLE II. From top to bottom: Single-site matrix elements  $\langle d_m^5 | c_{xz,\sigma}^\dagger | d_n^4 \rangle$ ,  $\langle d_m^3 | c_{xz,\sigma} | d_n^4 \rangle$ , and  $\langle d_m^3 | c_{xy,\sigma} | d_n^4 \rangle$  (bottom) for double occupancy of the  $xy$  orbital in the  $d^4$  initial state. The allowed value of spin  $\sigma$  is given in brackets for each finite entry.

matrix elements are given by

$$\begin{aligned}
 & |M_{n,n'}^{m,m'}|^2 \\
 &= \sum_{k,k'} \left| \langle d_{k,m}^3 d_{k',m'}^5 | \sum_{\tau,\tau',\sigma} t_{\tau\tau'} c_{k',\tau'\sigma}^\dagger c_{k,\tau\sigma} | d_{k,n}^4 d_{k',n'}^4 \rangle \right|^2 \\
 &= \sum_{k,k'} \left| - \sum_{\tau,\tau',\sigma} t_{\tau\tau'} \langle d_m^3 | c_{\tau\sigma} | d_n^4 \rangle_k \langle d_{m'}^5 | c_{\tau'\sigma}^\dagger | d_{n'}^4 \rangle_{k'} \right|^2.
 \end{aligned}$$

where  $t_{\tau\tau'}$  is the hopping matrix element between orbitals  $\tau$  and  $\tau'$  on adjacent sites,  $\sigma \in \{\uparrow, \downarrow\}$  refers to the electron spin, and  $kk' \in \{ij, ji\}$ . The restriction to nearest-neighbor sites is justified because of the small hopping matrix elements between further neighbors. The last line uses single-site matrix elements which facilitates the calculation. For double occupancy of the  $xy$  orbital in the ground state, the relevant single-site matrix elements are given in Tab. II.

### C. Cubic multiplets

Here we give the cubic multiplets that appear in Tab. II [28].

$$|t_{2g}^5(^2T_2, yz\sigma)\rangle = c_{yz\sigma}^\dagger c_{xz\uparrow}^\dagger c_{xz\downarrow}^\dagger c_{xy\uparrow}^\dagger c_{xy\downarrow}^\dagger |0\rangle \quad (20)$$

$$|t_{2g}^3(^4A_2, 3\sigma)\rangle = c_{xz\sigma}^\dagger c_{yz\sigma}^\dagger c_{xy\sigma}^\dagger |0\rangle \quad (21)$$

$$\begin{aligned}
 |t_{2g}^3(^4A_2, \sigma)\rangle &= \frac{1}{\sqrt{3}} \left( c_{xz\sigma}^\dagger c_{yz\sigma}^\dagger c_{xy-\sigma}^\dagger + c_{xz-\sigma}^\dagger c_{yz\sigma}^\dagger c_{xy\sigma}^\dagger \right. \\
 &\quad \left. + c_{xz\sigma}^\dagger c_{yz-\sigma}^\dagger c_{xy\sigma}^\dagger \right) |0\rangle. \quad (22)
 \end{aligned}$$

$$\begin{aligned}
 |t_{2g}^3(^2E, a, \sigma)\rangle &= \frac{1}{\sqrt{6}} \left( -2 c_{xz\sigma}^\dagger c_{yz\sigma}^\dagger c_{xy-\sigma}^\dagger + c_{xz-\sigma}^\dagger c_{yz\sigma}^\dagger c_{xy\sigma}^\dagger \right. \\
 &\quad \left. + c_{xz\sigma}^\dagger c_{yz-\sigma}^\dagger c_{xy\sigma}^\dagger \right) |0\rangle \quad (23)
 \end{aligned}$$

$$|t_{2g}^3(^2T_1, yz\sigma)\rangle = \frac{1}{\sqrt{2}} \left[ c_{yz\sigma}^\dagger c_{xy\uparrow}^\dagger c_{xy\downarrow}^\dagger - c_{xz\uparrow}^\dagger c_{xz\downarrow}^\dagger c_{yz\sigma}^\dagger \right] |0\rangle \quad (24)$$

---

[1] W. Witczak-Krempa, G. Chen, Y. B. Kim, and L. Balents, *Correlated Quantum Phenomena in the Strong Spin-Orbit Regime*, Annu. Rev. Condens. Matter Phys. **5**, 57 (2014).

[2] J. G. Rau, E. K.-H. Lee, and H.-Y. Kee, *Spin-Orbit Physics Giving Rise to Novel Phases in Correlated Systems: Iridates and Related Materials*, Annu. Rev. Condens. Matter Phys. **7**, 195 (2016).

[3] R. Schaffer, E. K.-H. Lee, B.-J. Yang, and Y. B. Kim, *Recent progress on correlated electron systems with strong spin-orbit coupling*, Rep. Prog. Phys. **79**, 094504 (2016).

[4] T. Takayama, J. Chaloupka, A. Smerald, G. Khaliullin, and H. Takagi, *Spin-Orbit-Entangled Electronic Phases in 4d and 5d Transition-Metal Compounds*, J. Phys. Soc. Jpn. **90**, 062001 (2021).

[5] D. I. Khomskii and S. V. Streltsov, *Orbital Effects in Solids: Basics, Recent Progress, and Opportunities*, Chem. Rev. **121**, 2992 (2021).

[6] S. V. Streltsov and D. I. Khomskii, *Jahn-Teller effect and spin-orbit coupling: friends or foes?*, Phys. Rev. X **10**, 031043 (2020).

[7] S. Nakatsuji, S.-I. Ikeda, and Y. Maeno,  *$Ca_2RuO_4$ : New Mott Insulators of Layered Ruthenate*, J. Phys. Soc. Japan, **66**, 1868 (1997).

[8] C. S. Alexander, G. Cao, V. Dobrosavljevic, S. McCall, J. Crow, E. Lochner, and R. Guertin, *Destruction of the Mott insulating ground state of  $Ca_2RuO_4$  by a structural transition*, Phys. Rev. B **60**, R8422 (1999).

[9] M. Braden, G. André, S. Nakatsuji, and Y. Maeno, *Crystal and magnetic structure of  $Ca_2RuO_4$ : Magnetoelastic coupling and the metal-insulator transition*, Phys. Rev. B **58**, 847 (1998).

[10] F. Nakamura, M. Sakaki, Y. Yamanaka, S. Tamaru, T. Suzuki, and Y. Maeno, *Electric-field-induced metal maintained by current of the Mott insulator  $Ca_2RuO_4$* , Sci. Rep. **3**, 2536 (2013).

[11] R. Okazaki, Y. Nishina, Y. Yasui, F. Nakamura, T. Suzuki, and I. Terasaki, *Current-Induced Gap Suppression in the Mott Insulator  $Ca_2RuO_4$* , J. Phys. Soc. Jpn. **82**, 103702 (2013).

[12] J. Zhang, A. S. McLeod, Q. Han, X. Chen, H. A. Bechtel, Z. Yao, S. N. Gilbert Corder, T. Ciavatti, T. H. Tao, M. Aronson, G. L. Carr, M. C. Martin, C. Sow, S. Yonezawa, F. Nakamura, I. Terasaki, D. N. Basov, A. J. Millis, Y. Maeno, and M. Liu, *Nano-Resolved Current-Induced Insulator-Metal Transition in the Mott Insulator  $Ca_2RuO_4$* , Phys. Rev. X **9**, 011032 (2019).

[13] J. Bertinshaw, N. Gurung, P. Jorba, H. Liu, M. Schmid, D. T. Mantadakis, M. Daghofer, M. Krautloher, A. Jain, G. H. Ryu, O. Fabelo, P. Hansmann, G. Khaliullin, C. Pfleiderer, B. Keimer, and B. J. Kim, *Unique Crystal Structure of  $Ca_2RuO_4$  in the Current Stabilized Semimetallic State*, Phys. Rev. Lett. **123**, 137204 (2019).

[14] K. Jenni, F. Wirth, K. Dietrich, L. Berger, Y. Sidis, S. Kunkemöller, C. P. Grams, D. I. Khomskii, J. Hemberger, and M. Braden, *Evidence for current-induced phase coexistence in  $Ca_2RuO_4$  and its influence on magnetic order*, Phys. Rev. Materials **4**, 085001 (2020).

[15] S. Nakatsuji and Y. Maeno, *Switching of magnetic coupling by a structural symmetry change near the Mott transition in  $Ca_{2-x}Sr_xRuO_4$* , Phys. Rev. B **62**, 6458 (2000).

[16] S. Nakatsuji and Y. Maeno, *Quasi-two-dimensional Mott transition system  $Ca_{2-x}Sr_xRuO_4$* , Phys. Rev. Lett. **84**, 2666 (2000).

[17] S. Nakatsuji, D. Hall, L. Balicas, Z. Fisk, K. Sugahara, M. Yoshioka, and Y. Maeno, *Heavy-mass Fermi liquid near a ferromagnetic instability in layered ruthenates*, Phys. Rev. Lett. **90**, 137202 (2003).

[18] S. Nakatsuji, V. Dobrosavljevic, D. Tanaskovic, M. Minakata, H. Fukazawa, and Y. Maeno, *Mechanism of hopping transport in disordered Mott insulators*, Phys. Rev. Lett. **93**, 146401 (2004).

[19] J. P. Carlo, T. Goko, I. M. Gat-Malureanu, P. L. Russo, A. T. Savici, A. A. Aczel, G. J. MacDougall, J. A. Rodriguez, T. J. Williams, G. M. Luke, C. R. Wiebe, Y. Yoshida, S. Nakatsuji, Y. Maeno, T. Taniguchi, and Y. J. Uemura, *New magnetic phase diagram of  $(Sr,Ca)_2RuO_4$* , Nature Mat. **11**, 323 (2012).

[20] S. Riccò, M. Kim, A. Tamai, S. McKeown Walker, F. Y. Bruno, I. Cucchi, E. Cappelli, C. Besnard, T. K. Kim, P. Dudin, M. Hoesch, M. J. Gutmann, A. Georges, R. S. Perry, and F. Baumberger, *In situ strain tuning of the metal-insulator-transition of  $Ca_2RuO_4$  in angle-resolved photoemission experiments*, Nat.

Commun. **9**, 4535 (2018).

[21] O. Friedt, M. Braden, G. André, P. Adelmann, S. Nakatsuji, and Y. Maeno, *Structural and magnetic aspects of the metal-insulator transition in  $Ca_{2-x}Sr_xRuO_4$* , Phys. Rev. B **63**, 174432 (2001).

[22] G. Khaliullin, *Excitonic Magnetism in Van Vleck-type  $d^4$  Mott Insulators*, Phys. Rev. Lett. **111**, 197201 (2013).

[23] A. Akbari and G. Khaliullin, *Magnetic Excitations in Spin-Orbit Coupled  $d^4$  Mott Insulator on Square Lattice*, Phys. Rev. B **90**, 035137 (2014).

[24] S. Kunkemöller, D. Khomskii, P. Steffens, A. Piovano, A. A. Nugroho, and M. Braden, *Highly Anisotropic Magnon Dispersion in  $Ca_2RuO_4$ : Evidence for Strong Spin-Orbit Coupling*, Phys. Rev. Lett. **115**, 247201 (2015).

[25] S. Kunkemöller, E. Komleva, S. V. Streltsov, S. Hoffmann, D. I. Khomskii, P. Steffens, Y. Sidis, K. Schmalzl, and M. Braden, *Magnon dispersion in  $Ca_2Ru_{1-x}Ti_xO_4$ : Impact of spin-orbit coupling and oxygen moments*, Phys. Rev. B **95**, 214408 (2017).

[26] A. Jain, M. Krautloher, J. Porras, G. H. Ryu, D. P. Chen, D. L. Abernathy, J. T. Park, A. Ivanov, J. Chaloupka, G. Khaliullin, B. Keimer, and B. J. Kim, *Higgs mode and its decay in a two-dimensional antiferromagnet*, Nat. Phys. **13**, 633 (2017).

[27] S.-M. Souliou, J. Chaloupka, G. Khaliullin, G. Ryu, A. Jain, B. J. Kim, M. Le Tacon, and B. Keimer, *Raman Scattering from Higgs Mode Oscillations in the Two-Dimensional Antiferromagnet  $Ca_2RuO_4$* , Phys. Rev. Lett. **119**, 067201 (2017).

[28] G. Zhang and E. Pavarini, *Mott transition, spin-orbit effects, and magnetism in  $Ca_2RuO_4$* , Phys. Rev. B **95**, 075145 (2017).

[29] G. Zhang and E. Pavarini, *Higgs mode and stability of xy-orbital ordering in  $Ca_2RuO_4$* , Phys. Rev. B **101**, 205128 (2020).

[30] P. M. Sarte, C. Stock, B. R. Ortiz, K. H. Hong, and S. D. Wilson, *Van Vleck excitons in  $Ca_2RuO_4$* , Phys. Rev. B **102**, 245119 (2020).

[31] S. Mohapatra and A. Singh, *Magnetic reorientation transition in a three orbital model for  $Ca_2RuO_4$  – interplay of spin-orbit coupling, tetragonal distortion, and Coulomb interactions*, J. Phys.: Condens. Matter **32**, 485805 (2020).

[32] T. Feldmaier, P. Strobel, M. Schmid, P. Hansmann, and M. Daghofer, *Excitonic magnetism at the intersection of spin-orbit coupling and crystal-field splitting*, Phys. Rev. Res. **2**, 033201 (2020).

[33] P. Strobel, F. Aust, and M. Daghofer, *Magnetic phases for strongly correlated  $t_{2g}^4$  electrons on the square lattice: Impact of spin-orbit coupling and crystal field*, Phys. Rev. B **104**, 115148 (2021).

[34] J. H. Jung, Z. Fang, J. P. He, Y. Kaneko, Y. Okimoto, and Y. Tokura, *Change of Electronic Structure in  $Ca_2RuO_4$  Induced by Orbital Ordering*, Phys. Rev. Lett. **91**, 056403 (2003).

[35] Z. Fang, N. Nagaosa, and K. Terakura, *Orbital-dependent phase control in  $Ca_{2-x}Sr_xRuO_4$  ( $0 \leq x \leq 0.5$ )*, Phys. Rev. B **69**, 045116 (2004).

[36] E. Gorelov, M. Karolak, T. O. Wehling, F. Lechermann, A. I. Lichtenstein, and E. Pavarini, *Nature of the Mott transition in  $Ca_2RuO_4$* , Phys. Rev. Lett. **104**, 226401 (2010).

[37] T. Mizokawa, L. H. Tjeng, G. A. Sawatzky, G. Ghiringhelli, O. Tjernberg, N. B. Brookes, H. Fukazawa, S. Nakatsuji, and Y. Maeno, *Spin-Orbit Coupling in the Mott Insulator  $Ca_2RuO_4$* , Phys. Rev. Lett. **87**, 077202 (2001).

[38] B. Yuan, J. P. Clancy, A. M. Cook, C. M. Thompson, J. Greedan, G. Cao, B. C. Jeon, T. W. Noh, M. H. Upton, D. Casa, T. Gog, A. Paramekanti, and Y.-J. Kim, *Determination of Hund's coupling in 5d oxides using resonant inelastic x-ray scattering*, Phys. Rev. B **95**, 235114 (2017).

[39] S. Fuchs, T. Dey, G. Aslan-Cansever, A. Maljuk, S. Wurmehl, B. Büchner, and V. Kataev, *Unraveling the Nature of Magnetism of the  $5d^4$  Double Perovskite  $Ba_2YIrO_6$* , Phys. Rev. Lett. **120**, 237204 (2018).

[40] D.I. Khomskii, *Transition metal compounds*, Cambridge University Press (2014).

[41] O. N. Meetei, W. S. Cole, M. Randeria, and N. Trivedi, *Novel magnetic state in  $d^4$  Mott insulators*, Phys. Rev. B **91**, 054412 (2015).

[42] D. Sutter, C.G. Fatuzzo, S. Moser, M. Kim, R. Fittipaldi, A. Vecchione, V. Granata, Y. Sassa, F. Cossalter, G. Gatti, M. Grioni, H.M. Rønnow, N.C. Plumb, C.E. Matt, M. Shi, M. Hoesch, T.K. Kim, T.-R. Chang, H.-T. Jeng, C. Jozwiak, A. Bostwick, E. Rotenberg, A. Georges, T. Neupert, and J. Chang, *Hallmarks of Hund's coupling in the Mott insulator  $Ca_2RuO_4$* , Nature Comm. **8**, 15176 (2017).

[43] A. Klosinski, D. V. Efremov, J. van den Brink, and K. Wohlfeld, *Photoemission spectrum of  $Ca_2RuO_4$ : Spin polaron physics in an  $S=1$  antiferromagnet with anisotropies*, Phys. Rev. B **101**, 035115 (2020).

[44] H. Gretarsson, H. Suzuki, H. Kim, K. Ueda, M. Krautloher, B. J. Kim, H. Yavas, G. Khaliullin, and B. Keimer, *Observation of spin-orbit excitations and Hund's multiplets in  $Ca_2RuO_4$* , Phys. Rev. B **100**, 045123 (2019).

[45] G. Khaliullin, P. Horsch, and A. M. Oleś, *Theory of optical spectral weights in Mott insulators with orbital degrees of freedom*, Phys. Rev. B **70**, 195103 (2004).

[46] A. M. Oleś, G. Khaliullin, P. Horsch, and L. F. Feiner, *Fingerprints of spin-orbital physics in cubic Mott insulators: Magnetic exchange interactions and optical spectral weights*, Phys. Rev. B **72**, 214431 (2005).

[47] G. Khaliullin, *Orbital Order and Fluctuations in Mott Insulators*, Prog. Theor. Phys. Suppl. **160**, 155 (2005).

[48] Z. Fang, N. Nagaosa, and K. Terakura, *Anisotropic optical conductivities due to spin and orbital ordering in  $LaVO_3$  and  $YVO_3$ : First-principles studies*, Phys. Rev. B **67**, 035101 (2003).

[49] S. Miyasaka, Y. Okimoto, and Y. Tokura, *Anisotropy of Mott-Hubbard Gap Transitions due to Spin and Orbital Ordering in  $LaVO_3$  and  $YVO_3$* , J. Phys. Soc. Jpn. **71**, 2086 (2002).

[50] N. N. Kovaleva, A. V. Boris, C. Bernhard, A. Kulakov, A. Pimenov, A. M. Balbashov, G. Khaliullin, and B. Keimer, *Spin-Controlled Mott-Hubbard Bands in  $LaMnO_3$  Probed by Optical Ellipsometry*, Phys. Rev. Lett. **93**, 147204 (2004).

[51] J. S. Lee, M. W. Kim, and T. W. Noh, *Optical excitations of transition-metal oxides under the orbital multiplicity effects*, New J. Phys. **7**, 147 (2005).

[52] R. Rauer, M. Rübbhausen, and K. Dörr, *Magnetic-order induced spectral-weight redistribution in  $La_{0.7}(Sr,Ca)_{0.3}MnO_3$* , Phys. Rev. B **73**, 092402 (2006).

[53] A. Gössling, M. W. Haverkort, M. Benomar, H. Wu, D. Senff, T. Möller, M. Braden, J. A. Mydosh, and M. Grüninger, *Mott-Hubbard versus charge-transfer behavior in  $LaSrMnO_4$  studied via optical conductivity*, Phys. Rev. B **77**, 035109 (2008).

[54] A. Gössling, R. Schmitz, H. Roth, M. W. Haverkort, T. Lorenz, J. A. Mydosh, E. Müller-Hartmann, and M. Grüninger, *Mott-Hubbard exciton in the optical conductivity of  $YTiO_3$  and  $SmTiO_3$* , Phys. Rev. B **78**, 075122 (2008).

[55] N. N. Kovaleva, A. M. Oleś, A. M. Balbashov, A. Maljuk, D. N. Argyriou, G. Khaliullin, and B. Keimer, *Low-energy Mott-Hubbard excitations in  $LaMnO_3$  probed by optical ellipsometry*, Phys. Rev. B **81**, 235130 (2010).

[56] A. S. Moskvin, and R. V. Pisarev, *Optical spectroscopy of charge transfer transitions in multiferroic manganites, ferrites*,

*and related insulators*, Low Temp. Phys. **36**, 489 (2010).

[57] J. Reul, A. A. Nugroho, T. T. M. Palstra, and M. Grüninger, *Probing orbital fluctuations in  $RV\text{O}_3$  ( $R = \text{Y, Gd, or Ce}$ ) by ellipsometry*, Phys. Rev. B **86**, 125128 (2012).

[58] J. Reul, L. Fels, N. Qureshi, K. Shportko, M. Braden, and M. Grüninger, *Temperature-dependent optical conductivity of layered  $\text{LaSrFeO}_4$* , Phys. Rev. B **87**, 205142 (2013).

[59] C. Monney, V. Bisogni, K.-J. Zhou, R. Kraus, V. N. Strocov, G. Behr, J. Malek, R. Kuzian, S.-L. Drechsler, S. Johnston, A. Revcolevschi, B. Büchner, H. M. Rønnow, J. van den Brink, J. Geck, and T. Schmitt, *Determining the Short-Range Spin Correlations in the Spin-Chain  $\text{Li}_2\text{CuO}_2$  and  $\text{CuGeO}_3$  Compounds Using Resonant Inelastic X-Ray Scattering*, Phys. Rev. Lett. **110**, 087403 (2013).

[60] E. Benckiser, L. Fels, G. Ghiringhelli, M. Moretti Sala, T. Schmitt, J. Schlappa, V. N. Strocov, N. Mufti, G. R. Blake, A. A. Nugroho, T. T. M. Palstra, M. W. Haverkort, K. Wohlfeld, and M. Grüninger, *Orbital superexchange and crystal field simultaneously at play in  $\text{YVO}_3$ : Resonant inelastic x-ray scattering at the V L edge and the O K edge*, Phys. Rev. B **88**, 205115 (2013).

[61] L. J. Sandilands, C. H. Sohn, H. J. Park, S.Y. Kim, K. W. Kim, J. A. Sears, Y.-J. Kim, and T. W. Noh, *Optical probe of Heisenberg-Kitaev magnetism in  $\alpha\text{-RuCl}_3$* , Phys. Rev. B **94**, 195156 (2016).

[62] A. Koitzsch, E. Müller, M. Knupfer, B. Büchner, D. Nowak, A. Isaeva, T. Doert, M. Grüninger, S. Nishimoto, and J. van den Brink, *Low-temperature enhancement of ferromagnetic Kitaev correlations in  $\alpha\text{-RuCl}_3$* , Phys. Rev. Materials **4**, 094408 (2020).

[63] J.S. Lee, Y.S. Lee, T.W. Noh, S.-J. Oh, J. Yu, S. Nakatsuji, H. Fukazawa, and Y. Maeno, *Electron and Orbital Correlations in  $\text{Ca}_{2-x}\text{Sr}_x\text{RuO}_4$  Probed by Optical Spectroscopy*, Phys. Rev. Lett. **89**, 257402 (2002).

[64] D. E. Aspnes, *Approximate solution of ellipsometric equations for optically biaxial crystals*, J. Opt. Soc. Am. **70**, 1275 (1980).

[65] C. G. Fatuzzo, M. Dantz, S. Fatale, P. Olalde-Velasco, N. E. Shaik, B. Dalla Piazza, S. Toth, J. Pelliciari, R. Fittipaldi, A. Vecchione, N. Kikugawa, J. S. Brooks, H. M. Rønnow, M. Grioni, Ch. Rüegg, T. Schmitt, and J. Chang, *Spin-orbit-induced orbital excitations in  $\text{Sr}_2\text{RuO}_4$  and  $\text{Ca}_2\text{RuO}_4$ : A resonant inelastic x-ray scattering study*, Phys. Rev. B **91**, 155104 (2015).

[66] L. Das, F. Forte, R. Fittipaldi, C. G. Fatuzzo, V. Granata, O. Ivashko, M. Horio, F. Schindler, M. Dantz, Y. Tseng, D. E. McNally, H. M. Rønnow, W. Wan, N. B. Christensen, J. Pelliciari, P. Olalde-Velasco, N. Kikugawa, T. Neupert, A. Vecchione, T. Schmitt, M. Cuoco, and J. Chang, *Spin-Orbital Excitations in  $\text{Ca}_2\text{RuO}_4$  Revealed by Resonant Inelastic X-Ray Scattering*, Phys. Rev. X **8**, 011048 (2018).

[67] S. Sugano, Y. Tanabe, and H. Kamimura, *Multiplets of Transition-Metal Ions in Crystals*, Pure and Applied Physics Vol. **33** (Academic, New York, 1970).

[68] A. Georges, Luca de'Medici, and J. Mravlje, *Strong Correlations from Hund's Coupling*, Ann. Rev. Condens. Matt. Phys. **4**, 137 (2013).

[69] For the  $t_{2g}$  shell one finds  $U_{t_{2g}} = F^0 + (4/49)(F^2 + F^4)$  and  $J_{H,t_{2g}} = (3/49)F^2 + (20/441)F^4$  [68], where  $F^0$ ,  $F^2$ , and  $F^4$  are Slater parameters. As common, we use parameters referring to the entire  $d$  shell, with  $U = F^0$  and  $J_H \approx J_{H,t_{2g}}/0.77$  [68]. Both approaches nominally yield the same expressions for the Mott-Hubbard excitation energies given in Tab. I.

[70] D. Pincini, L. S. I. Veiga, C. D. Dashwood, F. Forte, M. Cuoco, R. S. Perry, P. Bencok, A. T. Boothroyd, and D. F. McMorrow, *Tuning of the  $\text{Ru}^{4+}$  ground-state orbital population in the  $4d^4$  Mott insulator  $\text{Ca}_2\text{RuO}_4$  achieved by La doping*, Phys. Rev. B **99**, 075125 (2019).

[71] I. Zegkinoglou, J. Stempfer, C. S. Nelson, J. P. Hill, J. Chakhalian, C. Bernhard, J. C. Lang, G. Srayer, H. Fukazawa, S. Nakatsuji, Y. Maeno, and B. Keimer, *Orbital Ordering Transition in  $\text{Ca}_2\text{RuO}_4$  Observed with Resonant X-Ray Diffraction*, Phys. Rev. Lett. **95**, 136401 (2005).

[72] E. Sarvestani, G. Zhang, E. Gorelov, and E. Pavarini, *Effective masses, lifetimes, and optical conductivity in  $\text{Sr}_2\text{RuO}_4$  and  $\text{Sr}_3\text{Ru}_2\text{O}_7$ : Interplay of spin-orbit, crystal-field, and Coulomb tetragonal tensor interactions*, Phys. Rev. B **97**, 085141 (2018). Two typos in the coefficients were pointed out in Ref. [73].

[73] G. Zhang and E. Pavarini, *Spin-Orbit and Coulomb Effects in Single-Layered Ruthenates*, Phys. Status Solidi RRL **12**, 1800211 (2018).

[74] J. Lotze and M. Daghofer, *Suppression of effective spin-orbit coupling by thermal fluctuations in spin-orbit coupled antiferromagnets*, Phys. Rev. B **104**, 045125 (2021).